Front dynamics and pinning-depinning phenomenon in spatially periodic media

F. Haudin,[1] R. G. Elías,[2] R. G. Rojas,[3] U. Bortolozzo,[1] M. G. Clerc,[2] and S. Residori[1]
[1]*INLN, Université de Nice-Sophia Antipolis, CNRS, 1361 route des Lucioles, 06560 Valbonne, France*
[2]*Departamento de Física, Facultad de Ciencias Físicas y Matemáticas, Universidad de Chile, Casilla 487-3, Santiago, Chile*
[3]*Instituto de Física, Pontificia Universidad Católica de Valparaíso, Casilla 4059, Valparaíso, Chile*
(Received 5 February 2010; published 13 May 2010)

Front propagation in one- and two-dimensional spatially modulated media is studied both experimentally and theoretically. The *pinning-depinning* phenomenon, long ago predicted by Pomeau [Physica D **23**, 3 (1986)], is obtained and verified experimentally in a nematic liquid-crystal cell under various configurations of optical forcing. The front dynamics is characterized with respect to the different forcing parameters and the observations are compared with numerical simulations of a full model for the tilt angle of the liquid crystals under optical feedback. A spatially forced dissipative ϕ^4 model is derived near the points of nascent bistability. From this model we derive analytical results that account qualitatively for the observed front dynamics and pinning range. Localized structures of different sizes and shapes are found to exist inside the pinning range and experimentally proved to be stable states of the spatially forced system.

DOI: 10.1103/PhysRevE.81.056203 PACS number(s): 05.45.−a, 45.70.Qj, 47.54.−r

I. INTRODUCTION

In out of equilibrium systems, different states can coexist for a given range of parameters. Interfaces between such metastable states appear in the form of propagating fronts and give rise to a rich spatiotemporal dynamics [1–7]. Front dynamics occurs in systems as different as walls separating magnetic domains [8], directed solidification process [9], nonlinear optical systems [10–13], oscillating chemical reactions [14], or population dynamics [15–17]. From the point of view of dynamical system theory, in one-dimensional (1D) spatial dimension a front is a nonlinear solution that is identified in the comoving frame system as a heteroclinic orbit linking two spatially extended states [7,18].

The dynamics of the interface depends on the nature of the states that are connected. In the case of a front connecting a stable and an unstable state, called a Fisher-Kolmogorov-Petrosvky-Piskunov (FKPP) front [15,19], the velocity is not unique but determined by the initial conditions. The situation is different for a front connecting two stable states. In this case, a gradient system tends to develop the most stable state, in order to minimize its energy, so that the front always propagates toward the most energetically favored state. It exists only as one point in parameter space for which the front is motionless, which is usually called the Maxwell point, and is the point for which the two states have exactly the same energy [20].

The above scenario changes drastically when one considers a system with discrete reflection symmetry, which can, therefore, possess two equivalent states. As a consequence of the discrete symmetry, the interfaces, or domain walls, connecting such equivalent states are generically at rest. Indeed, the two connected states are "energetically" equivalent. However, under spontaneous breaking of the parity symmetry, these fronts can acquire a nonzero asymptotic speed. This phenomenon is the denominated Ising-Bloch transition [21] and has been observed in such different systems as ferromagnetic systems [22], liquid crystals (LCs) [23,24], chemical reactions [25], and nonlinear optical cavities [26]. Gradient or variational systems do not exhibit this phenomenon, because the front speed is proportional to the energy difference between the two equivalent states. On the other hand, the dynamics of a nongradient system can be decomposed in two parts, a dissipative and a remnant part, such that a Lyapunov functional—*nonequilibrium potential*—characterizes the dissipative dynamics [27]. The steady states of the nonequilibrium system minimize the nonequilibrium potential, whereas the remnant dynamics is responsible for the nontrivial behavior of stationary states, such as oscillations, chaos, and so forth. In the same way, the front propagation occurring through the Ising-Bloch transition is a consequence of the remnant dynamics. Due to the universal nature of domain-wall propagation, the transition from a resting to a moving front is, in this context, usually denominated as a nonvariational or nonequilibrium Ising-Bloch transition [28,29].

A different situation is that of a front connecting a homogeneous and a periodic state, for which the existence of a *pinning range* was predicted by Pomeau [1] more than 20 years ago. In this case, a pinning-depinning phenomenon is expected to occur as a result of the competition between a symmetry breaking of the global energy that tends to favor the front propagation in one direction and spatial modulations that tend to block the front by introducing local potential barriers at the front core dynamics [30,31]. Depending on the dominating effect, the front can either stay motionless—blocked over a large range, therefore called the pinning range—or propagate with periodic leaps apart from it. Starting from a critical value of the control parameter, the pinning-depinning transition occurs by a loss of stability of the pinned front.

The existence of a pinning range, and associated pinning-depinning phenomenon, has a fundamental relevance in numerous domains where front propagation is involved. As examples, we can cite vibrated fluids [32], chemical reactions [14,33], microfluidic chips [34], wetting of microstructured surfaces [35], control of the motility of bacteria [36], and growth of self-assembly monolayers [37], just to cite a few. Indeed, spatial discreteness and spatial modulations can be

seen as the bases for a wealth of life behaviors, where the emergence of complexity results from the microscopic granularity of the system [38]. As for the experimental studies of the pinning-depinning phenomenon, only a few approaches have been proposed up to date. In a two-dimensional (2D) spatially forced system, an experimental characterization of front propagation has shown the anisotropy of the front velocity [39]; however, the issue of a pinning range was not addressed. Only recently, by employing a 1D spatially forced liquid-crystal system, the experimental demonstration of the existence of a pinning range has been achieved [40].

In this paper, we extend our previous findings by reporting an experimental and theoretical study of 1D and 2D pinning-depinning phenomena in a nematic liquid-crystal light valve with optical feedback. Starting from fronts between homogeneous states, spatial light modulations are introduced by using a spatial light modulator (SLM). In this way, uniform states are transformed into patterned ones and pinning effects appear spontaneously in the system. Numerical simulations of a full model for the average liquid-crystal tilt angle under optical feedback have been performed, providing a good agreement with the experimental results. Close to the points of nascent bistability, a spatially forced dissipative ϕ^4 model has been derived, which is able to capture analytically the main features of front propagation over the spatially modulated medium. Finally, we show that localized structures of different sizes and shapes exist inside the pinning range and are experimentally proved to be stable states of the spatially modulated system.

The paper is organized as follows. In Sec. II the experimental setup is described and in Sec. III the full model for the liquid-crystal light valve (LCLV) with optical feedback is presented. Section IV presents the 1D spatially forced model, the experimental evidence of the pinning-depinning phenomenon, and the influence of the different forcing parameters. Section V deals with the 2D dynamics, showing the possibility of introducing anisotropic as well as isotropic front propagation over differently structured grids and associated pinning-depinning effects. In Sec. VI we show that localized structures of arbitrary shape can be stabilized inside the pinning range of 2D spatially modulated systems. Finally, Sec. VII presents the conclusions.

II. EXPERIMENTAL SETUP

The experimental setup comprises a LCLV inserted in an optical feedback loop. The LCLV consists of a thin film of nematic liquid crystals interposed in between a glass plate and a photoconductive material over which a dielectric mirror is deposed. The confining surfaces of the cell are treated for a planar anchoring of the liquid-crystal molecules (nematic director $\vec{n}$ parallel to the walls) [41]. Transparent electrodes deposited over the cell walls allow us to apply an external voltage V_0 across the liquid-crystal layer. Molecules tend to orient along the direction of the applied electric field, which—on its turn—changes locally and dynamically by following the illumination distribution present on the photoconductive wall of the cell. When liquid-crystal molecules reorient, because of their birefringence, they induce a change in the refractive index [42]. Thus, the LCLV acts as a Kerr medium, providing for the reflected beam a phase variation $\varphi = kdn_2 I_w$ proportional to the intensity I_w of the beam incoming on its photoconductive side. Here, d is the thickness of the nematic layer, $k = 2\pi/\lambda$ is the optical wave number, and n_2 is the equivalent nonlinear coefficient.

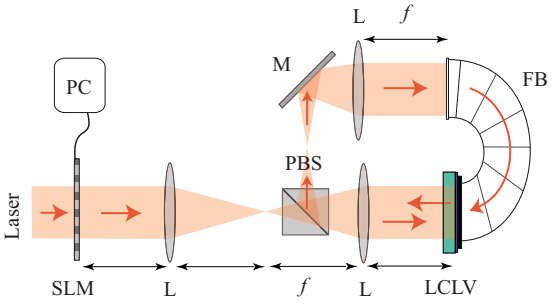

FIG. 1. (Color online) Schematic experimental setup: FB is an optical fiber bundle, $f = 25$ cm is the focal length of each lens L, M is a mirror, PBS is a polarizing beam splitter, and PC is the computer driving the SLM.

A schematic of the experiment is displayed in Fig. 1. Similar setups have been previously used in various different configurations for the study of spatiotemporal phenomena and pattern formation in nonlinear optics [13,43–46]. Here, we focus on the front dynamics that occurs when bistability is introduced between homogeneous states [10]. The LCLV is illuminated by an expanded He-Ne laser beam ($\lambda = 632.8$ nm), with 3 cm transverse diameter, linearly polarized along the vertical direction. Once shone onto the LCLV, the beam is reflected back by the dielectric mirror deposed on the rear side of the cell and, thus, sent in the feedback loop. A polarizing beam splitter (PBS), a mirror M, and an optical fiber bundle FB are used to close the loop and to send the beam back to the photoconductive side of the LCLV. The liquid-crystal director is oriented at 45°. The PBS introduces polarization interference between the ordinary and extraordinary waves propagating in the liquid-crystal layer, thus ensuring the bistability between differently orientated states of the liquid-crystal molecules [13]. Together with the diffraction-free situation, this is the main ingredient necessary to get *normal fronts* connecting spatially uniform stable extended states. These fronts correspond to different orientations of the liquid crystals and appear in the transverse direction of the beam propagation as moving interfaces between different levels of the light intensity [10].

In the feedback loop, a self-imaging configuration is obtained by using two lenses L of the same focal length $f = 25$ cm, placed in such a way that the rear and front sides of the LCLV are conjugate planes. Thanks to this configuration the free propagation length in the feedback loop is set to zero; hence, we have a diffraction-free situation. A SLM is placed on the optical path of the input beam and a third lens L, of the same focal length $f = 25$ cm, provides a 1:1 imaging of the SLM onto the front side of the LCLV. The SLM is a liquid-crystal display, 1 in. diagonal size, with a 1024 $\times$ 768 pixels, each coded in 8 bits of intensity level, interfaced with a personal computer PC. By using a dedicated

software, intensity masks are produced and sent to the SLM, which acts as a programmable filter able to impose arbitrary spatial modulations on the input beam profile. Either 1D or 2D intensity forcing is introduced by using appropriate intensity masks.

To obtain 1D profiles, masks were sent to the SLM with a zero-level intensity except on a narrow channel of 150 μm width and 2.5 mm length. In the channel, the intensity is set either to a uniform level A or spatially modulated with an amplitude B and wavelength p, providing a general expression for the input beam profile $I_{in}(x)=A+B\sin(2\pi x/p)$, where both A and B are controlled by changing the transmittance of the SLM. Here, the intensity is expressed in gray levels, from 0 to 255, as delivered by the SLM. For a uniform mask of 185 gray values, a typical value of the input intensity is $I_{in}=0.84$ mW/cm^2. To obtain 2D profiles, masks $I(x,y)$ were produced with a transverse extension and with different grid symmetries. Both in the 1D and 2D cases, the front dynamics is controlled by adjusting the parameter of the imposed spatial modulations as well as by varying the external voltage V_0 applied to the LCLV.

III. LCLV MODEL EQUATIONS

The model describing the evolution of the average orientation tilt angle of the liquid-crystal molecules was first introduced in [47]. It consists of a diffusive and relaxation equation for the average director tilt $\theta(x,t)$, $0\le\theta\le\pi/2$, coupled with an equation for the feedback light intensity I_w [13]. In the case of zero diffraction length in the feedback loop, the equation for I_w can easily be solved, and the full LCLV model reads as

$$\tau_{LC}\partial_t\theta = l^2\nabla^2\theta - \theta + \begin{cases} 0, & V_{LC} < V_{FT} \\ \dfrac{\pi}{2}\left(1-\sqrt{\dfrac{\Gamma V_{FT}}{V_{LC}(\theta)}}\right), & V_{LC}\ge V_{FT}, \end{cases} \tag{1}$$

where $\tau_{LC}=30$ ms is the LC relaxation time, $l=30$ μm is the electric coherence length, $\nabla_\perp^2$ is the transverse Laplacian, and

$$V_{LC}(\theta) = \Gamma V_0 + \alpha I_w \tag{2}$$

is the effective voltage applied to the liquid crystals, with $V_{FT}=3.2$ V_{rms} as the threshold for the Fréedericksz transition, $\Gamma\sim 0.3$ as the overall impedance of the LCLV dielectric layers, and $\alpha\sim 5.5$ V cm^2/mW as a phenomenological parameter summarizing, in the linear approximation, the response of the photoconductor.

The light intensity reaching the photoconductor is

$$I_w = I_{in}[1-\cos(\Delta\varphi)], \tag{3}$$

where $\Delta\varphi=\beta\cos^2\theta$ is the overall phase shift experienced by the light traversing the LC layer, $\beta=2kd\Delta n$ with $d=15$ μm as the thickness of the nematic layer, $\Delta n=0.2$ as the LC birefringence, and $k=2\pi/\lambda$ with $\lambda=632.8$ nm.

If one does not consider the optical feedback, model (1) describes a linear diffusive and relaxation dynamics, which characterizes the Fréedericksz transition for the liquid-crystal orientation under the application of an external field [41]. In our case, the equilibrium state θ_c satisfies

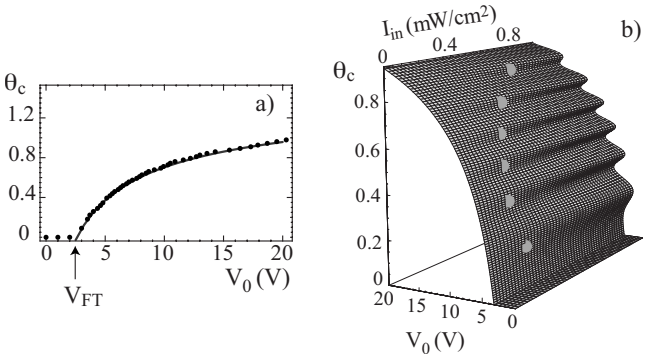

FIG. 2. (a) Equilibrium average director tilt θ_c as a function of the applied voltage V_0 in the absence of optical feedback; circles are experimental points and the solid line is a best fit with model (1). (b) The multivalued function $\theta_c(V_0,I_{in})$ representing the equilibrium average director tilt when the optical feedback is present; shaded areas mark the locations of the nascent bistability points.

$$\theta_c = \begin{cases} 0, & V_{LC} < V_{FT} \\ \dfrac{\pi}{2}\left(1-\sqrt{\dfrac{\Gamma V_{FT}}{V_{LC}}}\right), & V_{LC}\ge V_{FT}, \end{cases} \tag{4}$$

that is, molecules are characterized by an average vertical inclination $\theta_c=0$ when the applied voltage is below the critical value V_{FT} for the Fréedericksz transition to occur, whereas they acquire a nonzero average tilt when the voltage exceeds this threshold value. As illustrated in Fig. 2(a), near the critical value V_{FT} the inclination tilt increases as the square root of the voltage. Then, saturation takes place when all the molecules are in average aligned along the direction of the applied field.

In the absence of optical feedback, the Fréedericksz transition described by model (1) is of second order type. The above scenario changes drastically when one considers the optical feedback. In this case, liquid-crystal molecules interact with themselves through the optical loop and the relaxation dynamics becomes of nonlinear nature. As a consequence, the Fréedericksz transition becomes of first order type [10]. By considering $V_0>V_{FT}$, and by substituting into Eq. (1) the optical feedback intensity [Eq. (3)], we obtain the expression for the average equilibrium director tilt θ_c, which reads as

$$\theta_c = \frac{\pi}{2}\left(1-\sqrt{\frac{\Gamma V_{FT}}{\Gamma V_0 + \alpha I_{in}[1-\cos(\beta\cos^2\theta_c)]}}\right). \tag{5}$$

In Fig. 2(b) the average equilibrium director tilt is plotted as a function of the applied voltage V_0 and input intensity I_{in}, which are the two control parameters of the experiments. As highlighted by the figure, for sufficiently large values of the input intensity the surface describing the steady-state solution becomes folded. Close to the folding points, the system shows different branches of bistability, that is, it is characterized by more than one equilibrium state. Therefore, depend-

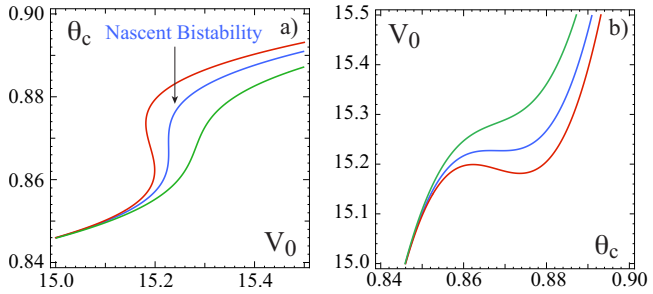

FIG. 3. (Color online) (a) Equilibrium average director tilt θ_c as a function of the applied voltage V_0 and at fixed input intensities I_{in}=0.38, 0.41, and 0.43 mW/cm^2 for the lower (green), middle (blue), and upper (red) curves, respectively. (b) Same graph for inverted axis.

ing on the initial condition, the molecular tilt may take different values for the same set of parameters. Due to the transverse spatial extension of the liquid-crystal layer, one expects to find domains with different inclinations of the molecules and, thus, a rich dynamical behavior associated with the presence of fronts connecting these domains.

Determination of the points of nascent bistability

To have a simple description of the fronts dynamics in the system under consideration, we first study the dynamics of model (1) around the emergence of bistability, i.e., when the function $\theta_c(V_0, I_{in})$ becomes multivalued. At this purpose, we express Eq. (5) as

$$V_0 = \frac{V_{FT}}{\left(1 - \frac{2\theta_c}{\pi}\right)^2} - \frac{\alpha I_{in}}{\Gamma}[1 - \cos(\beta \cos^2 \theta_c)], \tag{6}$$

and from this relation we determine the values of parameters for the emergence of bistability. Indeed, in the parameter space, the above expression generates a folded surface from which one can geometrically infer the points of nascent bistability. In fact, θ_c becomes multivalued when the function $V_0(\theta_c, I_{in})$ has a saddle point.

To illustrate this property we plot in Fig. 3(a) the equilibrium average director tilt as a function of V_0 and for three different values of the input intensity taken close to a point of nascent bistability. By exchanging the axis of the graph, as represented in Fig. 3(b), the multivalued function $\theta_c(V_0)$ becomes a single-valued function $V_0(\theta_c)$. By confronting the two graphs, we can easily see that the nascence of bistability is characterized by the appearance of a saddle point for the $V_0(\theta_c)$ function. Moreover, around the saddle point $V_0(\theta_c)$ creates two new extreme points that determine the width of the bistability region. From the viewpoint of the theory of dynamical systems the emergence of bistability reveals the existence of an imperfect pitchfork bifurcation [48]. On the other hand, from the viewpoint of catastrophe theory the emergence of new equilibria is related to the cusp catastrophe and the nascent bistability point is associated with the tip of the cusp [49].

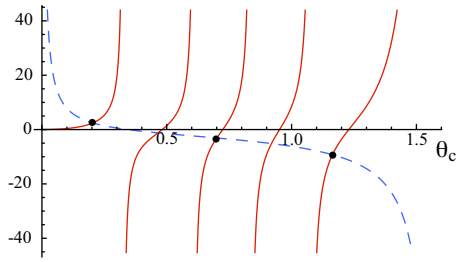

FIG. 4. (Color online) Left-hand (dashed blue curve) and right-hand (solid red curve) sides of Eq. (8) for β=14; the points of nascent bistability, marked by the filled circles, are the interception points of the two curves that correspond to positive intensity.

To find the saddle points of the $V_0(\theta_c)$ function we impose the conditions $dV_0/d\theta_c=0$, $d^2V_0/d^2\theta_c=0$ and, after straightforward calculations, we obtain the relations

$$I_{in} = \frac{-\pi^2 \Gamma V_{FT}}{2\alpha\beta(\pi/2 - \theta_c)^3 \sin(2\theta_c)\sin(\beta \cos^2 \theta_c)}, \tag{7}$$

$$\frac{3}{\frac{\pi}{2} - \theta_c} - 2 \cot 2\theta_c = -\beta \sin(2\theta_c)\cot(\beta \cos^2 \theta_c). \tag{8}$$

The first expression [Eq. (7)] gives the critical value of I_{in} for which θ_c becomes multivalued. The second expression [Eq. (8)] is an algebraic equation that depends only on the parameter β and determines all the points of nascent bistability. The curves in Fig. 4 are the left- and right-hand sides of Eq. (8), calculated for β=14. The interception points of the two curves correspond to all the points of nascent bistability that can be found for this value of β. However, only half of them have physical significance because the other half correspond to negative values of the intensity.

By taking into account the constraint that the intensity must be positive and considering that the cotangent function is π periodic, we have that the actual number of points of nascent bistability is equal to the next smallest integer of $\beta/2\pi$. For the values considered in the experiment β is about 54, then one expects to find eight points of nascent bistability in the entire (V_0, I_{in}) parameter space, a prediction that is confirmed by the experiment. In Fig. 4 the actual points of nascent bistability are marked by filled circles. Once a point of nascent bistability is identified, one can determine the critical values (V_0^c, I_{in}^c) of the voltage and input intensity for which θ_c becomes multivalued and, then, characterize the front dynamics in the vicinity of those values.

IV. 1D SPATIALLY MODULATED SYSTEMS

A. Forced model and pinning-depinning phenomenon

As depicted in Fig. 3, the dynamics near a nascent bistability point is described by a vector field governed by a cubic nonlinearity. Hence, close to a given point of nascent bistability, $I_{in} \equiv I_{in}^c$, and $V_0 \equiv V_0^c$, we can approximate the average director tilt field by the expression

$$\theta(\vec{r},t) \approx \theta_c + \frac{\phi(\vec{r},t)}{\phi_0}, \tag{9}$$

where $\phi(\vec{r},t)$ is an order parameter that accounts for the dynamics around the point of nascent bistability and $\phi_0^2 \equiv 2\beta \cos 2\theta_c \cot(\beta \cos^2 \theta_c) + (4+\beta^2 \sin 2\theta_c)/3 - 2/(\pi/2 - \theta_c)^2$ is a normalization constant introduced to simplify the equation for the field ϕ.

Introducing the above expression into Eq. (1), considering the 1D forced case and developing in Taylor series by keeping the cubic terms, after straightforward algebraic calculations, we can reduce the full LCLV model to a forced dissipative ϕ^4 model, which reads as

$$\tau \partial_t \phi = \eta + \varepsilon\phi - \phi^3 + l^2 \partial_{xx}\phi + (b + c\phi)\sin\left(\frac{2\pi x}{p}\right), \tag{10}$$

where b, c, and p are the forcing parameters, with p as the spatial period of the forcing grid. The various coefficient η, ϵ, b, and c can be expressed as functions of the different experimental parameters and read as

$$\eta \equiv \frac{2\alpha}{\pi^2 V_{FT}}[1 - \cos(\beta \cos^2 \theta_0)](\pi/2 - \theta_0)^3\{\Gamma I_{in} - \Gamma I_c + \alpha[1 - \cos(\beta \cos^2 \theta_0)](V_0 - V_c)\},$$

$$\varepsilon \equiv \frac{12}{\pi^2 V_{FT}}[(\pi/2 - \theta_0)^2 (V_0 - V_c)] + \frac{12}{\pi^2 V_{FT}}\left[\left(\frac{\pi^2 V_{FT}}{12} - (\pi/2 - \theta_0)^2\right)(I_{in} - I_c)/I_c\right],$$

$$b \equiv \frac{2\alpha B}{\pi^2 \Gamma V_{FT}}[1 - \cos(\beta \cos^2 \theta_0)](\pi/2 - \theta_0)^3,$$

$$c \equiv \frac{B}{I_c}\left[1 - \frac{12 V_0}{\pi^2 V_{FT}}(\pi/2 - \theta_0)^2\right],$$

where B is the amplitude of the forcing.

It is instructive to write the above model in a potential form

$$\tau \partial_t \phi = -\frac{\partial F}{\partial \phi}, \tag{11}$$

where

$$F = -\int \left[\eta\phi + \varepsilon\frac{\phi^2}{2} - \frac{\phi^4}{4} - \frac{l^2}{2}(\partial_{xx}\phi)^2\right] dx \tag{12}$$

is the Lyapunov functional for the unforced case ($b=c=0$), which has a potential associated of the form

$$V(\phi) = \eta\phi + \varepsilon\frac{\phi^2}{2} - \frac{\phi^4}{4}.$$

Then the dynamics of the previous model is characterized by the minimization of the potential F. This situation corresponds to an imperfect extended pitchfork bifurcation [6,7,48] and admits front solutions connecting the two stable states that coincide with the minima of the potential.

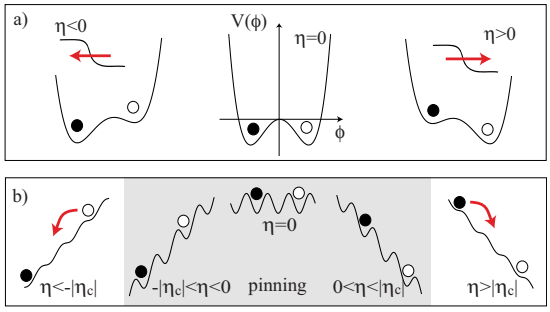

FIG. 5. (Color online) Evolution with η of the potential $V(\phi)$ for the (a) unforced and (b) spatially forced cases. (a) For $\eta<0$ or $\eta>0$, the front propagates toward the most favored state, as indicated by the red arrow, and stays motionless only at the Maxwell point, $\eta=0$. (b) The front is pinned over a large range of parameters and propagates by periodical leaps only when η exceeds a critical value η_c.

The analytical expression of the motionless front connecting asymptotically the stable state $\sqrt{\varepsilon}$ with the other stable state $-\sqrt{\varepsilon}$ can be easily calculated and reads as ($\eta=0$)

$$\phi_k(x - x_0) = \pm\sqrt{\varepsilon}\tanh[\sqrt{\varepsilon l^2/2}(x - x_0)]. \tag{13}$$

The front always propagates toward the most energetically favorable state, which is defined by the sign of η. This situation is depicted in Fig. 5(a), where the potential is plotted, together with the corresponding direction of front propagation, for negative and positive η (left and right graphs, respectively). It exists only as one point in the parameter space, the so-called Maxwell point [7,20], for which the interface is immobile because the two states have the same energy, and this occurs for $\eta=0$ (central graph). When a spatial forcing is introduced ($b \sim c \neq 0$), the uniform states become periodic and the front exhibits a pinning range, that is, it is motionless in a large interval of parameters. A qualitative representation of this effect is represented in Fig. 5(b). Because of the local potential wells introduced by the spatial forcing, the front remains trapped beyond the potential barriers and does not propagate until η exceeds a critical value η_c (central shaded area). Once this happens, the front propagates by leaps over the discontinuous potential, moving toward the most favorable state on the respective side of the pinning range (left and right graphs).

To study analytically the effect of the forcing, we consider the ansatz $\phi(x,t) = \phi_k(x - x_0(t)) + w(x,x_0)$, where x_0 is the position of the front core, that is, the region of space where the front has the highest spatial variations. Introducing the previous ansatz in Eq. (10), linearizing in w, and imposing a solvability condition, after straightforward calculations we derive [50]

$$\dot{x}_0 = -\frac{3\eta}{\sqrt{2\varepsilon}} - \gamma(p)\sin\left(\frac{2\pi}{p}x_0 + \chi\right), \tag{14}$$

from which we see that the front speed has a constant term plus an oscillatory part. The amplitude of the oscillation is

$$\gamma(p) = 2\pi^2 \,\mathrm{cosech}(\sqrt{2}\pi^2/p)\sqrt{9b^2p^2 + 2c^2\pi^2}/2p^3, \quad (15)$$

and $\tan\chi = \sqrt{2}c\pi/3bp$. The front is motionless in the range of parameters for which the first term is smaller than the amplitude of the periodic term, which defines the pinning range $\eta_- \leq \eta \leq \eta_+$, with the critical values being $\eta_\pm \equiv \pm\sqrt{2\varepsilon}\gamma(p)/3$. Outside this region, the front propagates with an oscillatory speed. In order to compute the average front speed we can integrate the above equation [Eq. (14)] and obtain

$$x_0(t) = x_0(t_0) + p/2\pi \arctan[\tan(p/2\pi\sqrt{9\eta^2/\gamma^2 2\varepsilon - 1}t) \times \sqrt{3\eta + \gamma\sqrt{2\varepsilon}}/\sqrt{3\eta - \gamma\sqrt{2\varepsilon}}]. \quad (16)$$

The above expression can be rewritten in the following form:

$$\tan\left[\frac{2\pi[x_0(t) - x_0(t_0)]}{p}\right] = \frac{\sqrt{3\eta + \gamma\sqrt{2\varepsilon}}}{\sqrt{3\eta - \gamma\sqrt{2\varepsilon}}}\tan(p/2\pi\sqrt{9\eta^2/\gamma^2 2\varepsilon - 1}t). \quad (17)$$

Hence, we have the equality of two periodic functions of period 2π. If λ and τ are, respectively, the spatial and temporal periods, then they satisfy the relation

$$\lambda = p, \quad \tau = \mp\sqrt{9\eta^2/\gamma^2 2\varepsilon - 1}/p,$$

and the average front speed can be defined as

$$\left\langle \frac{dx_0}{dt} \right\rangle = \frac{\lambda}{\tau} = \mp\sqrt{9\eta^2/\gamma^2 2\varepsilon - 1}.$$

As an alternative way, we can rewrite the above expression as [50]

$$\left\langle \frac{dx_0}{dt} \right\rangle = \mp\frac{3\sqrt{2}}{2}\eta\sqrt{1 - \left(\frac{\eta_\pm}{\eta}\right)^2}. \quad (18)$$

For $|\eta| < |\eta_\pm|$ the above formula is imaginary, i.e., the front speed is zero. Close to $\eta_\pm$, the above formula recovers the dynamical behavior expected for a saddle-node bifurcation, with the front speed increasing as a square root of η, as predicted by the following formula:

$$\langle dx_0/dt \rangle \approx \mp 3\sqrt{(\eta - \eta_\pm)\eta_\pm}. \quad (19)$$

However, for large η, the average front speed behaves as a linear function of η.

In Fig. 6 the bifurcation structure of the front speed numerically obtained from the ϕ^4 model is compared with the analytical expression of Eq. (18), showing a good agreement. The forcing parameters are $A=1$, $B=0.2$, and $p=0.05L_x$, with $L_x=800$ as the number of integration points. Figure 7 displays the bifurcation structure of the average front speed $\langle dx_0/dt \rangle$ numerically calculated for the full LCLV model [Eq. (1)] and for the same forcing parameters as above. The solid lines on the same figures are the theoretical fits with Eq. (18). Thus, when one compares the bifurcation structure of the front speed obtained from the full LCLV model with the analytical expression of Eq. (18), a good agreement is also found.

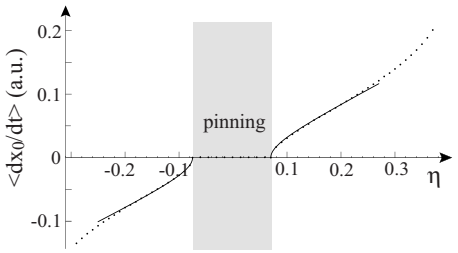

FIG. 6. Bifurcation structure of the average front speed for the ϕ^4 model [Eq. (10)]; a.u. is arbitrary units. Points are numerical simulations and solid lines are theoretical fits with Eq. (18).

In summary, a large pinning range clearly appears when spatial modulations are introduced in the system. The ϕ^4 model provides a simplified description around the points of nascent bistability, where we can understand the mechanism of front propagation and perform analytical calculations. These results, when compared with the full LCLV model, show a remarkable agreement.

B. Experimental observations of the pinning-depinning phenomenon

The front dynamics in the 1D spatially forced case has been characterized by using intensity masks of zero-level intensity everywhere except on a narrow channel (width $D=150$ μm and length 2.5 mm), where the intensity has the expression $I(x)=A+B\sin(2\pi x/p)$. The resulting input intensity I_{in} in front of the LCLV is spatially modulated as $I_{in}=I_0+b_0\sin(2\pi x/p)$, where both I_0 and b_0 can be controlled by changing A and B. I_0 is measured when imposing a uniform 2D masks with A gray value. In the set of measurements presented here we have fixed $I_0=0.9$ mW/cm^2 and $b_0=0.1$ mW/cm^2. This average intensity is kept constant. As previously seen, the response of the liquid-crystal molecules depends on I_{in} and V_0. Here, the control parameter chosen to tune the front dynamics is V_0, playing the role of a symmetry breaking parameter like the η parameter in the ϕ^4 model.

Once identified the range of V_0 values corresponding to the bistable region, where two different molecular orientation states coexist, we have characterized the dynamics of the normal fronts propagating over a uniform background. For different V_0 voltages, the front speed is measured by recording with a charge-coupled device camera the interface evolution over the channel. In the absence of spatial forcing, the

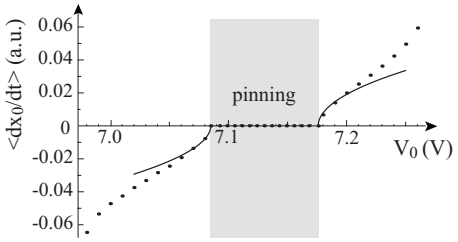

FIG. 7. Bifurcation structure of the average front speed $\langle dx_0/dt \rangle$ for the full LCLV model with optical feedback (1); a.u. is arbitrary units. Points are numerical simulations and solid lines are theoretical fits with Eq. (18).

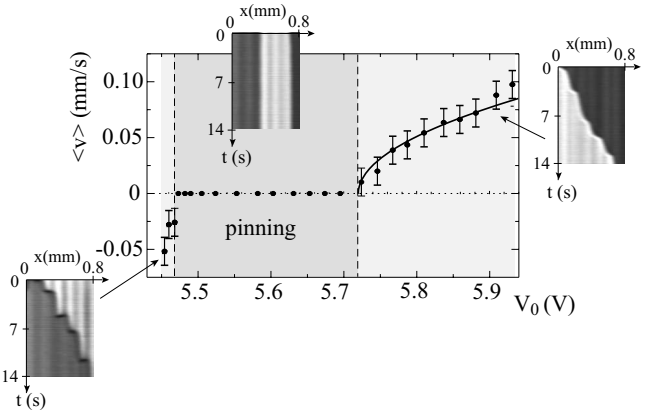

FIG. 8. Average front velocity $\langle v \rangle$ against the voltage V_0 in the spatially forced experiment; $A=210$, $B=15$, and $p=115$ μm; the light gray area is the bistable region, while the shaded darker area is the pinning range. Shown in the insets are the spatiotemporal plots of the front evolution before, inside, and beyond the pinning range.

most stable state tends to invade all the available space, developing an expanding or retracting front. The front speed evolves linearly with V_0, with its sign changing at the Maxwell point, the only point where the front is motionless [40]. When, with the SLM, we apply the spatially periodic forcing, the uniform states transform into patterns and the dynamics changes significantly. The front either stays motionless in a large region of parameters or outside this region propagates by periodical leaps. In Fig. 8 the average front velocity $\langle v \rangle$ is plotted against V_0 for a forcing wavelength $p=115$ μm. Due to the spatial forcing, the front is pinned over a large range of parameters, confirming Pomeau's prediction [1]: in order to propagate over a periodic medium the core of the front has to overcome a finite energy barrier. The experimentally observed pinning range is marked in the figure by the darkest shaded area, whereas the light gray area marks the region of bistability.

Outside the pinning range the front propagation occurs through periodical leaps and the front speed oscillates regularly. Most particularly, the pinning-depinning transition at the right or left side of the pinning range is a saddle-node bifurcation. The solid line in Fig. 8 represents the velocity calculated by using the theoretical prediction [Eq. (18)], which scales as the square root of η close to the pinning-depinning transition and linearly with η far from this transition. We can note that the experimental results are in a qualitative good agreement with the model. The region on the left side of the pinning range (retracting front) is very small; hence, it was not possible to accurately fit the speed of the front in this region.

C. Influence of the forcing parameters

The influence of the forcing parameters has been tested in various experimental measurements. As a first test, we have checked the influence of the intensity level around which the modulation is made. A was then set to 190, instead of 210 as in the previous measurements, and the input intensity I_0 was changed, correspondingly, from 0.9 to 0.8 mW/cm^2. By following the same procedure as before, we have constructed the bifurcation diagram of the average speed $\langle v \rangle$ with respect to V_0, as reported in Fig. 9. We note that the pinning range is shifted to higher values of V_0, which is consistent with the intensity-voltage characteristics of the LCLV [47].

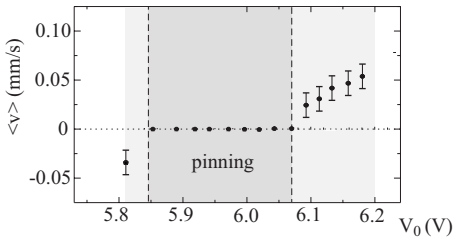

FIG. 9. Average front velocity $\langle v \rangle$ against the voltage V_0 in the spatially forced experiment; $A=190$, $B=15$, and $p=115$ μm; the light gray area is the bistable region, while the shaded darker area is the pinning range.

The main difference with respect to the previous case is the absence of leap propagation on the left side of the pinning range. When launching in this region an upper state as the initial condition, we observe that it relaxes locally to the lower state without oscillatory front motion. This behavior can be explained by considering that the modulation response of the system is more important for this forcing and, at higher modulation amplitudes, it may happen that the lower state collides with the uniform state and disappears by a saddle-node bifurcation. A similar behavior occurs for localized states when they are nucleated over a modulated background [51]. This phenomenon of relaxation onto the lower state at the left of the pinning range can be observed by numerical integration of the 1D model for the LCLV with a spatial forcing $I_{in}(x)=A+B\cos(\frac{2\pi x}{p})$.

Figure 10 shows numerical spatiotemporal plots obtained for increasing V_0 values and two different average intensities $A=3.5$ (upper row) and $A=4.5$ (lower row). For the lower value of V_0 (4.9 V), corresponding to Fig. 10(a), the system relaxes to the low state, whereas for $V_0=5.0$ and 5.1 V [Figs. 10(b) and 10(c)], the system is in the pinning range and there

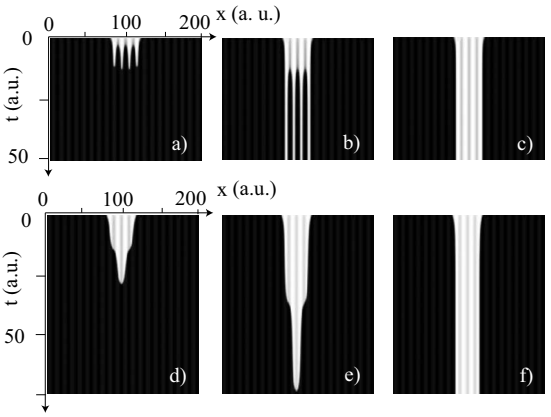

FIG. 10. Numerical spatiotemporal plots from the full LCLV model, showing for $A=3.5$ (upper row) and $A=4.5$ (lower row) the front evolution by changing V_0: $V_0=$(a) 4.9, (b) 5.0, (c) 5.1, (d) 4.5, (e) 4.6, and (f) 4.7 V. The other parameters are $\Gamma=1.0$, $\alpha=0.3$, $B=1.34$, and $p=10$.

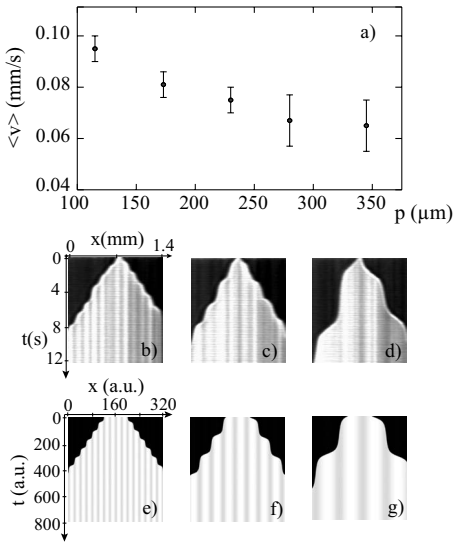

FIG. 11. (a) Average front speed $\langle v \rangle$ as a function of the forcing wavelength p. (b)–(d) Experimental and (e)–(g) numerical spatiotemporal plots showing the front propagating from a local initial condition at increasing forcing wavelength; p=(b) 115, (c) 173, and (d) 345 μm; p=(e) 20, (f) 40, and (g) 80; the other parameters are Γ=1.0, α=0.3, B=1.4, and V_0=5.35 V.

is no front propagation in between these two behaviors. On the other hand, for a higher average intensity A=4.5, the spatiotemporal plots show a front retracting by periodic leaps, as shown in Figs. 10(d) and 10(e) (V_0=4.5 and 4.6 V, respectively), and then a pinning range, as shown in Fig. 10(f) (V_0=4.7 V). As in the experiment, changing the average intensity value A leads to the disappearance of the front propagation at the left of the pinning range as well as decreasing A shifts the pinning range to higher V_0 voltage range.

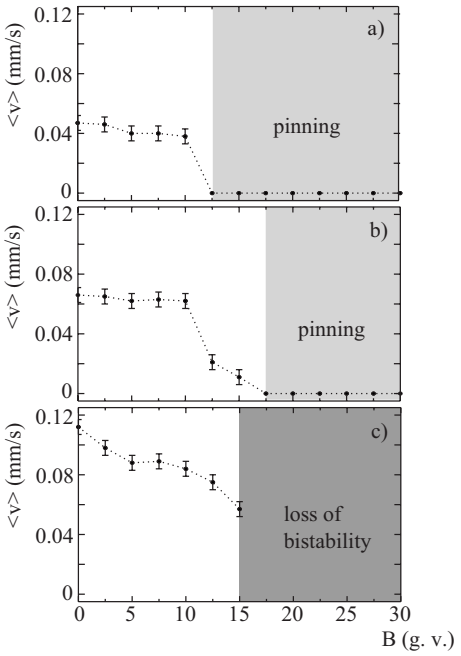

FIG. 12. Average front speed $\langle v \rangle$ measured as a function of the forcing modulation amplitude B for (a) V_0=5.54 V, (b) V_0 =5.6 V, and (c) V_0=5.7 V.

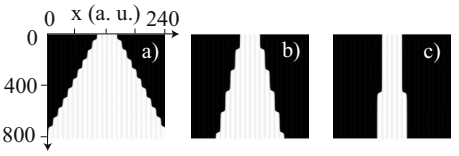

FIG. 13. Numerical spatiotemporal plots from the full LCLV model, showing the front evolution by changing the forcing amplitude B: B=(a) 0.9, (b) 0.94, and (c) 0.95. The other parameters are V_0=5.2 V, Γ=1.0, α=0.3, A=4.5, and p=10.

Then, the influence of the forcing wavelength at a constant V_0 voltage has been studied by changing the spatial period p of the grid delivered by the SLM. As p increases, the main qualitative effect is the increase in the pinning range and the decrease in the front speed. The experimentally measured change in the average front speed $\langle v \rangle$ as a function of p is reported in Fig. 11(a). Experimental and numerical spatiotemporal diagrams of the front propagating from a local initial condition are shown in Figs. 11(b)–11(g) for increasing forcing wavelength.

A final characterization of the pinning-depinning transition has been made for varying the amplitude B of the forcing modulation. The average front speed $\langle v \rangle$, measured as a function of B for three different values of V_0, is reported in Fig. 12. As can be seen in the figure, the smaller is V_0, the larger is the pinning range. For the largest value of V_0 no pinning occurs because the amplitude of the forcing is too important and the bistability is lost starting from B=15. Numerical spatiotemporal plots are shown in Fig. 13 for a fixed V_0 and by increasing the forcing amplitude B. We can note that, as B increases, the average front speed decreases until it reaches zero when entering the pinning range, which is in qualitative good agreement with the experimental results.

V. EXPERIMENTAL FRONT PROPAGATION IN SPATIALLY MODULATED 2D SYSTEMS

A. Stripe grid

As a first step, it is interesting to consider the extension in two dimensions of the 1D case presented above. To do this, the intensity mask sent to the SLM is made by designing a stripe grid uniform in the y direction, as shown in Fig. 14(a). The expression for the light intensity distribution reads as

$$I(x,y) = A + B[\sin(kx)], \tag{20}$$

where $k=2\pi/p$. The forcing wavelength is fixed at p =115 μm and we take as an initial condition a circular area

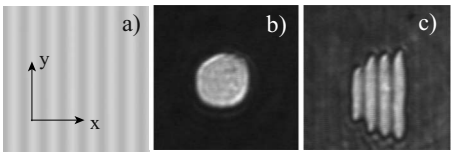

FIG. 14. (a) Stripe intensity mask delivered by the SLM; (b) circular initial condition used to generate the front; (c) resulting front propagating over the grid.

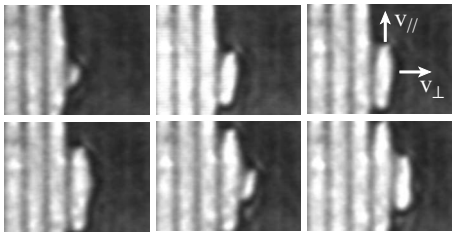

FIG. 15. Temporal sequence showing a front propagating over the stripe grid; V_0=6.0 V, A=195, B=15, and p=115 μm; the time delay between two successive snapshots is 0.8 s.

of 255 gray value level on a zero-level intensity background, as shown in Fig. 14(b). Once the initial condition is released, a front spontaneously propagates over the grid and along the stripe direction, as displayed in Fig. 14(c).

Because of the anisotropy of the forcing, one expects the dynamics of the front over the grid to be anisotropic, too. An example temporal sequence of the front propagation at the right side of the pinning range is shown in Fig. 15. The front presents a propagation characterized by discrete jumps in the direction perpendicular to the stripes, whereas the propagation occurs with a constant velocity along the parallel direction once a new island is nucleated on the closest stripe line of the underlying grid. Theoretical and numerical studies of propagation of striped patterns show that the propagation of the interface is anisotropic [52,53].

We have characterized experimentally the front propagation by measuring the average speed in both the parallel and perpendicular directions with respect to the stripes. The resulting bifurcation diagrams as a function of V_0 are displayed in Figs. 16(a) and 16(b), respectively. The speed in the direction parallel to the stripes, $\langle v_{\parallel} \rangle$, does not display a pinning range, and the front propagates uniformly on both sides of its

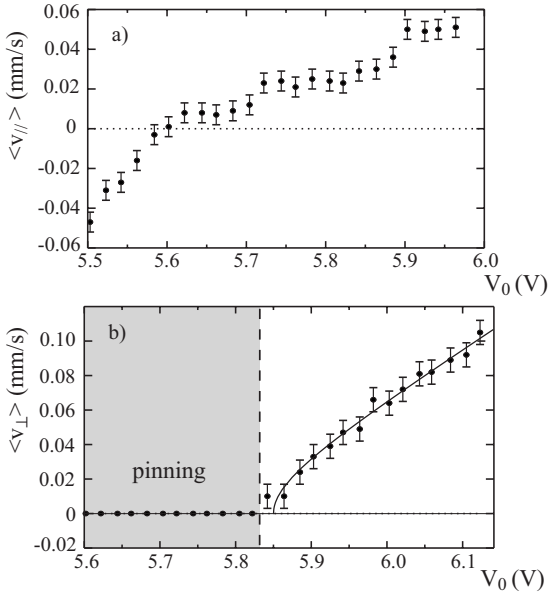

FIG. 16. Bifurcation diagram of the average front velocity (a) $\langle v_{\parallel} \rangle$ and (b) $\langle v_{\perp} \rangle$ in the stripe grid forced experiment; A=210, B=15, and p=115 μm. Solid line in (b) is a theoretical fit with Eq. (18).

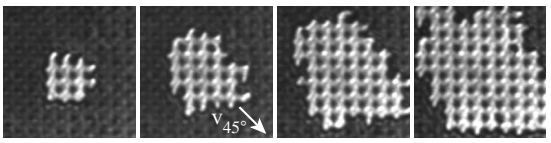

FIG. 17. Temporal sequence showing a front propagating over a square grid; V_0=5.7 V, A=190, B=30, and p=160 μm; the time delay between two successive snapshots is 3.2 s.

respective Maxwell point. On the other hand, the speed perpendicular to the stripes, $v_{\perp}$, shows a large pinning range and the front propagates with periodical leaps at the right of the pinning region. At the left side of the pinning range the propagation by leaps exists only for a very tiny region of parameters, before the loss of bistability. At the right side of the pinning range, we have fitted the front velocity with the theoretical expression [Eq. (18)]. The fit is represented by a solid line in Fig. 16(b). Again, we can see that Eq. (18) provides a very good agreement with the experimental data. For comparison, a fit with a square-root law, as predicted by the saddle node, has been tested and shown to provide a less accurate agreement, especially far from the pinning-depinning transition. We can, therefore, conclude that the ϕ^4 model gives a good qualitative description of the front dynamics close to the pinning range.

B. Square and hexagonal grids

We have seen that, by using a stripe grid, it is possible to pin the front in a given direction whereas it remains free to propagate in the perpendicular direction. Considering this, it is worth now to investigate the possibility of pinning the front in two directions by using 2D intensity masks with modulation along both directions, such as square or hexagonal grids.

To study the front dynamics over a square modulated medium, suitable intensity distributions were generated through the SLM, so that the input intensity takes the following expression:

$$I(x,y) = A + B[\cos(kx) + \cos(ky)],$$

with x as the horizontal direction, y as the vertical one, and $k=2\pi/p$, where p is the wavelength of the spatial modulation. The forcing wavelength is fixed at p=160 μm and the other forcing parameters are A=190 and B=30. For increasing V_0 we have measured the average front velocity along the diagonal direction, $\langle v_{45^\circ} \rangle$, as marked on the temporal sequence displayed in Fig. 17. The bifurcation diagram for $\langle v_{45^\circ} \rangle$ as a function of V_0 shows a clear pinning range, as displayed in Fig. 18. At the left or right side of the pinning range the front propagates by leaps, both in horizontal and vertical directions, with horizontal and vertical leaps alternating during the time.

We can proceed in a similar way by replacing the square modulation with a hexagonal grid and, thus, study the front dynamics over a hexagonally modulated medium. At this purpose, intensity profiles of the input beam were produced in the form

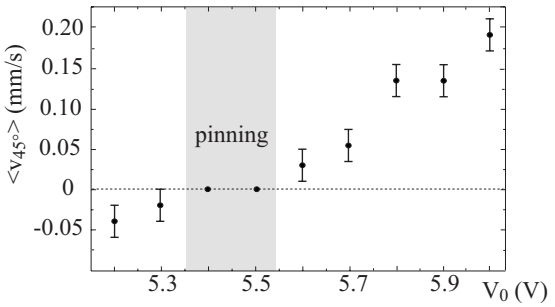

FIG. 18. Bifurcation diagram of the average velocity $\langle v_{45^\circ} \rangle$ of the front propagating along the diagonal of the square grid; $A=190$, $B=30$, and $p=160$ μm.

$$I(x,y) = A + B\left[\cos(kx) + \cos\left(\frac{1}{2}kx + \frac{\sqrt{3}}{2}ky\right)\right] + B\left[\cos\left(\frac{1}{2}kx - \frac{\sqrt{3}}{2}ky\right)\right],$$

with $k=2\pi/p$. Figure 19 displays a sequence of images showing how, starting from a circular initial condition, the generated front spontaneously propagates over a hexagonally modulated medium. We can note that the front moves by steps expanding along a discrete set of preferential directions, with these being dictated by the axis of symmetry of the underlying hexagonal grid.

As a generalization of this method more complex grids can be designed by adding more wave vectors, $\Sigma_i \vec{k}_i = 0$, with an appropriate phase matching condition. By sending the resulting grids to the SLM, the pinning-depinning phenomenon could be studied over arbitrarily spatially modulated media, for example, quasicrystal grids or superlattices. Similar methods could also be employed to study the behavior of ultracold atom clouds, or Bose-Einstein condensates, over arbitrarily complex or spatially modulated potentials [54].

VI. LOCALIZED STRUCTURES

Finally, it is interesting to investigate the possibility of using the pinning range in order to generate and stabilize localized structures of different sizes and different shapes. In the experiment, stable localized states can be induced by starting with a 2D suitable initial condition (square, circular, or uniform extended profile) and then switching it off over the spatially modulated medium.

To prove the existence of stable localized structures, by following the procedure described above we have taken either a square or a hexagonal grid, and we have set V_0 values in the pinning range of the front. Thanks to the bistability and to the pinning phenomenon, by locally applying a perturbation on the input intensity profile, it is possible to change the size of the initial pattern and then stabilize localized states formed by a different number of cells of the underlying grid. As an example, the alpaca picture displayed in Fig. 20 has been produced starting from a square initial condition over a square grid of wavelength $p=160$ μm. Another example is displayed in Fig. 21, where are shown a localized structure in the form of a large domain and, apart from this, a single-cell localized structure, both stabilized over a hexagonal grid of wavelength $p=150$ μm.

Thus, provided we fix the parameters in the pinning range of the fronts, localized structures are stable states of the 2D

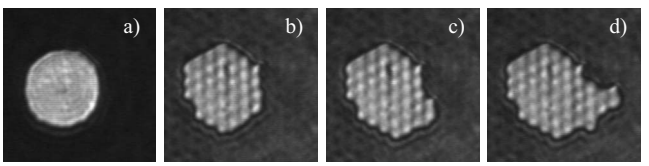

FIG. 19. Temporal sequence showing the spontaneous front evolution over a hexagonal grid; (a) is the circular initial condition and (b)–(d) are separated by a time delay of 4 s; $V_0=5.8$ V, $A=187.5$, $B=7.5$, and $p=130$ μm.

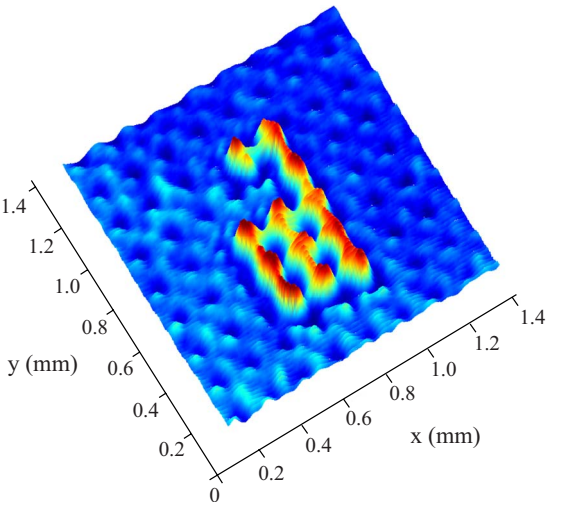

FIG. 20. (Color online) Three-dimensional intensity profile of a localized structure taking the form of an alpaca, stabilized over a square grid; $A=190$, $B=30$, $p=160$ μm, and $V_0=5.5$ V.

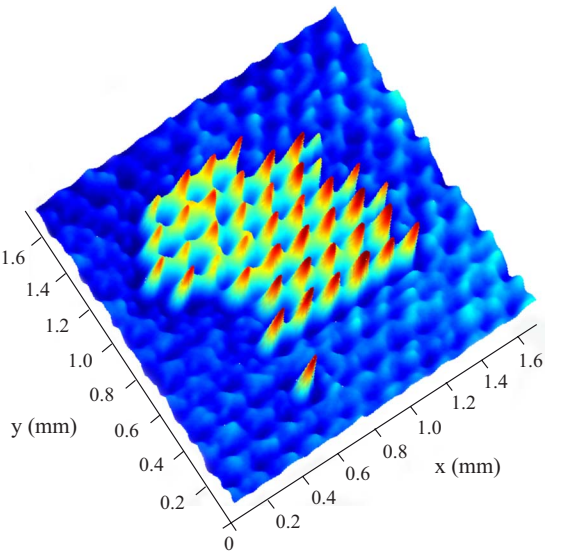

FIG. 21. (Color online) Three-dimensional intensity profile of a localized structure taking the form of a large domain, stabilized over a hexagonal grid together with a single-cell localized structure; $A=190$, $B=20$, $p=150$ μm, and $V_0=5.7$ V.

spatially forced system. Different shapes and symmetries of localized structures are expected to exist depending on the specific grid and initial conditions, which could be employed to extend the domain of possible applications of localized structures in optical control and storage [45,55–57].

VII. CONCLUSIONS

We have reported a detailed characterization of the 1D and 2D front dynamics in a spatially modulated medium and given evidence, both theoretically and experimentally, of the pinning-depinning phenomenon induced by the spatial forcing. The experiment consists of a LCLV with spatially modulated optical feedback. By adjusting the forcing parameters through a spatial light modulator, we have proved the possibility of controlling the front dynamics to a large extent. A significant pinning-depinning phenomenon has been obtained both in 1D and 2D spatially modulated systems.

Near the onset of bistability, we have derived an extended pitchfork bifurcation model with spatial forcing, which accounts for the main features of the front dynamics observed experimentally. In the 1D spatially forced system and in the 2D system forced with stripes we have shown a very good agreement between the experimental front speed and the theoretical prediction of the ϕ^4 model derived close to the points of nascent bistability. In 2D systems forced with square or hexagonal grids, we have shown that the front propagation becomes anisotropic, with the possibility of pinning the front along one or more specific directions coinciding with the symmetry axis of the underlying pattern.

Using a square or a hexagonal grid, we have shown that a voltage interval exists in the pinning range for which it is possible to stabilize localized structures of arbitrary size and shape, thus opening the possibility to use the spatially forced medium as an optical writing board. Further investigations are in progress to fully characterize the different localized states that can be stabilized in the pinning range.

ACKNOWLEDGMENTS

M.G.C. acknowledges the FONDECYT Project No. 1090045. R.G.R. thanks the FONDECYT Project No. 11080286. R.G.E. thanks the financial support of Becas de Estadías Cortas de Investigación de la Universidad de Chile. U.B. and S.R. thank the ANR Grant No. ANR-07-BLAN-0246-03, turbonde.

[1] Y. Pomeau, Physica D **23**, 3 (1986).
[2] G. Nicolis and I. Prigogine, *Self-Organization in Non-Equilibrium Systems* (John Wiley & Sons, New York, 1977).
[3] J. S. Langer, Rev. Mod. Phys. **52**, 1 (1980).
[4] P. Collet and J. P. Eckmann, *Instabilities and Fronts in Extended Systems* (Princeton University Press, Princeton, NJ, 1990).
[5] M. C. Cross and P. C. Hohenberg, Rev. Mod. Phys. **65**, 851 (1993).
[6] M. Cross and H. Greenside, *Pattern Formation and Dynamics in Nonequilibrium Systems* (Cambridge University Press, New York, 2009).
[7] L. M. Pismen, *Patterns and Interfaces in Dissipative Dynamics*, Springer Series in Synergetics (Springer, Berlin, 2006).
[8] A. H. Eschenfelder, *Magnetic Bubble Technology*, Springer Series of Solid States Science (Springer-Verlag, Berlin, 1983).
[9] T. Börzsönyi, S. Akamatsu, and G. Faivre, Phys. Rev. E **80**, 051601 (2009).
[10] M. G. Clerc, S. Residori, and C. S. Riera, Phys. Rev. E **63**, 060701(R) (2001).
[11] D. Gomila, P. Colet, G. L. Oppo, and M. San Miguel, Phys. Rev. Lett. **87**, 194101 (2001).
[12] M. G. Clerc *et al.*, Eur. Phys. J. D **28**, 435 (2004).
[13] S. Residori, Phys. Rep. **416**, 201 (2005).
[14] V. Petrov, Q. Ouyang, and H. L. Swinney, Nature (London) **388**, 655 (1997).
[15] R. A. Fisher, Ann. Eugen. **7**, 355 (1937).
[16] J. D. Murray, *Mathematical Biology I: An Introduction* (Springer, New York, 2002).
[17] M. G. Clerc, D. Escaff, and V. M. Kenkre, Phys. Rev. E **72**, 056217 (2005).
[18] W. van Saarloos and P. C. Hohenberg, Physica D **56**, 303 (1992).
[19] A. Kolmogorov, I. Petrovsky, and N. Piskunov, Bull. Univ. Moskou Ser. Int. Se. A **1**, 1 (1937).
[20] R. E. Goldstein, G. H. Gunaratne, L. Gil, and P. Coullet, Phys. Rev. A **43**, 6700 (1991).
[21] P. Coullet, J. Lega, B. Houchmanzadeh, and J. Lajzerowicz, Phys. Rev. Lett. **65**, 1352 (1990).
[22] L. N. Bulaevsky and V. L. Ginzburg, Sov. Phys. JETP **18**, 530 (1964).
[23] J. M. Gilli, M. Morabito, and T. Frisch, J. Phys. II **4**, 319 (1994).
[24] T. Kawagishi, T. Mizuguchi, and M. Sano, Phys. Rev. Lett. **75**, 3768 (1995).
[25] D. Haim, G. Li, Q. Ouyang, W. D. McCormick, H. L. Swinney, A. Hagberg, and E. Meron, Phys. Rev. Lett. **77**, 190 (1996).
[26] A. Esteban-Martin, V. B. Taranenko, J. Garcia, G. J. de Valcarcel, and E. Roldan, Phys. Rev. Lett. **94**, 223903 (2005).
[27] R. Graham and T. Tel, Phys. Rev. A **33**, 1322 (1986).
[28] D. Michaelis, U. Peschel, F. Lederer, D. V. Skryabin, and W. J. Firth, Phys. Rev. E **63**, 066602 (2001).
[29] M. G. Clerc, S. Coulibaly, and D. Laroze, Int. J. Bifurcation Chaos Appl. Sci. Eng. **19**, 2717 (2009).
[30] D. Bensimon, B. I. Shraiman, and V. Croquette, Phys. Rev. A **38**, 5461 (1988).
[31] M. G. Clerc, C. Falcon, and E. Tirapegui, Phys. Rev. Lett. **94**, 148302 (2005); Phys. Rev. E **74**, 011303 (2006).
[32] T. Epstein and J. Fineberg, Phys. Rev. Lett. **92**, 244502 (2004).
[33] M. E. Schwartz and T. H. Solomon, Phys. Rev. Lett. **100**, 028302 (2008).
[34] A. R. Thiam, N. Bremond, and J. Bibette, Phys. Rev. Lett.

102, 188304 (2009).
[35] M. Sbragaglia, A. M. Peters, C. Pirat, B. M. Borkent, R. G. H. Lammertink, M. Wessling, and D. Lohse, Phys. Rev. Lett. **99**, 156001 (2007).
[36] C. Douarche, A. Buguin, H. Salman, and A. Libchaber, Phys. Rev. Lett. **102**, 198101 (2009).
[37] J. F. Douglas *et al.*, Proc. Natl. Acad. Sci. U.S.A. **104**, 10324 (2007).
[38] N. M. Shnerb, Y. Louzoun, E. Bettelheim, and S. Solomon, Proc. Natl. Acad. Sci. U.S.A. **97**, 10322 (2000).
[39] J. Armero *et al.*, EPL **33**, 429 (1996); J. Armero, A. M. Lacasta, L. Ramirez-Piscina, J. Casademunt, J. M. Sancho, and F. Sagues, Phys. Rev. E **56**, 5405 (1997).
[40] F. Haudin, R. G. Elías, R. G. Rojas, U. Bortolozzo, M. G. Clerc, and S. Residori, Phys. Rev. Lett. **103**, 128003 (2009).
[41] P. G. De Gennes and J. Prost, *The Physics of Liquid Crystals*, 2nd ed. (Oxford Science Publications/Clarendon Press, Oxford, 1993).
[42] I. C. Khoo, *Liquid Crystals: Physical Properties and Nonlinear Optical Phenomena*, 2nd ed. (Wiley Interscience, New York, 2007).
[43] P. L. Ramazza, E. Benkler, U. Bortolozzo, S. Boccaletti, S. Ducci, and F. T. Arecchi, Phys. Rev. E **65**, 066204 (2002).
[44] U. Bortolozzo, R. Rojas, and S. Residori, Phys. Rev. E **72**, 045201(R) (2005).
[45] U. Bortolozzo and S. Residori, Phys. Rev. Lett. **96**, 037801 (2006).
[46] C. Cleff, B. Gütlich, and C. Denz, Phys. Rev. Lett. **100**, 233902 (2008).
[47] M. G. Clerc, A. Petrossian, and S. Residori, Phys. Rev. E **71**, 015205(R) (2005).
[48] S. H. Strogatz, *Nonlinear Dynamics and Chaos: With Applications to Physics, Biology, Chemistry and Engineering* (Addison-Wesley, Reading, MA, 1994).
[49] V. I. Arnold, *Catastrophe Theory* (Springer-Verlag, Berlin, 1984).
[50] R. Rojas, Ph.D. thesis, University of Nice-Sophia Antipolis, 2005 (http://tel.archives-ouvertes.fr).
[51] U. Bortolozzo, M. G. Clerc, C. Falcon, S. Residori, and R. Rojas, Phys. Rev. Lett. **96**, 214501 (2006).
[52] M. G. Clerc, D. Escaff, C. Falcon, and E. Tirapegui, Eur. Phys. J. Spec. Top. **143**, 171 (2007).
[53] M. G. Clerc, D. Escaff, and R. Rojas, EPL **83**, 28002 (2008).
[54] See, e.g., M. Greiner, O. Mandel, T. Esslinger, T. W. Hänsch, and I. Bloch, Nature (London) **415**, 39 (2002).
[55] F. Pedaci *et al.*, Appl. Phys. Lett. **92**, 011101 (2008).
[56] U. Bortolozzo, M. G. Clerc, and S. Residori, Phys. Rev. E **78**, 036214 (2008).
[57] U. Bortolozzo, M. G. Clerc, F. Haudin, R. Rojas, and S. Residori, Advances in Nonlinear Optics **2009**, 926810 (2009).